

Superbubble evolution including the star-forming clouds: Is it possible to reconcile LMC observations with model predictions?

Sergei Silich¹ and José Franco²

Received _____; accepted _____

arXiv:astro-ph/9905167v1 13 May 1999

¹Main Astronomical Observatory National Academy of Sciences of Ukraine, 252650 Kyiv, Golosiiv, Ukraine

(E-mail: silich@mao.kiev.ua)

²Instituto de Astronomía-UNAM, Apdo. Postal 70-264, 04510 México D. F., Mexico

(E-mail: pepe@astrocu.unam.mx)

ABSTRACT

Here we present a possible solution to the apparent discrepancy between the observed properties of LMC bubbles and the standard, constant density bubble model. A two-dimensional model of a wind-driven bubble expanding from a flattened giant molecular cloud is examined. We conclude that the expansion velocities derived from spherically symmetric models are not always applicable to elongated young bubbles seen almost face-on due to the LMC orientation. In addition, an observational test to differentiate between spherical and elongated bubbles seen face-on is discussed.

Subject headings: Galaxies: Kinematics and Dynamics — ISM:

Bubbles — ISM: Clouds — ISM: Kinematics and Dynamics — ISM;

Shock Waves — ISM: Structure — Magellanic Clouds

1. Introduction

Since the discovery of large shells and holes of neutral hydrogen in the Magellanic Clouds (see McGee & Milton 1966 and Westerlund & Mathewson 1966 for the LMC, and Hindman 1967 for the SMC), the Milky Way (Heiles 1979), and M31 (Brinks & Bajaja 1986), the study of interstellar bubbles has been extended to several nearby galaxies (see recent reviews by Brinks & Walter 1998, and Thilker 1998). The optical counterpart of these objects are the H_α ring-shaped nebulae (*e. g.* Boulesteix *et al.* 1974; Davies *et al.* 1976; Sivan 1977; Pellet *et al.* 1978; Meaburn 1980; Lozinskaya & Sitnik 1988), which are powered by young massive stars, and many HI bubbles are actually delineated by them. Thus a paradigm for bubble evolution driven by energy injection from massive stars was developed during the sixties and seventies by Pikel'ner (1968), Avedisova (1972), and Weaver *et al.* (1977). These original analytical models have been extended during the last two decades with 2D and 3D numerical simulations by Bisnovatyi-Kogan & Blinnikov (1982), Mac Low & McCray (1987), Palous (1992), and Silich (1992); see reviews by Tenorio-Tagle & Bodenheimer (1988) and Bisnovatyi-Kogan & Silich (1995).

A number of important processes affecting the expansion of shells have been studied during this time, including the effects of blowout and dynamical instabilities in decreasing density gradients (Mac Low *et al.* 1989; Tenorio-Tagle *et al.* 1990; García-Segura & McLow 1995a, 1995b), gravitational instabilities (McCray & Kafatos 1987; Ehlerova *et al.* 1997), ambient magnetic fields (Tomisaka 1990, 1998; Ferriere *et al.* 1991), galactic differential rotation (Palous 1992; Silich *et al.* 1996; Moreno *et al.* 1999), radiation pressure from field stars (Elmegreen & Chiang 1982; Franco *et al.* 1991), the impact of supernova fragments in expanding superbubble shells (Franco *et al.* 1993), the role of hydrodynamic ablation and thermal evaporation of ambient clouds (Hartquist *et al.* 1986; Arthur & Henney 1996; Silich *et al.* 1996), and photoionization from the central stars (Comeron 1997).

In principle, then, one could compare the predictions of a variety of different models (*i. e.*, the resulting bubble shapes, expansion velocities, column densities, X-ray luminosities, etc.) with the available observational data for holes and shells (*e. g.* Chu & Mac Low 1990; Silich *et al.* 1996; Mashchenko *et al.* 1998; Thilker *et al.* 1998). A direct comparison with observations, however, presents several problems because it is difficult to constraint most of the relevant model parameters (for instance, the energy input rate and the original density structure). Nonetheless, several steps have been done recently to overcome some of these questions, and additional problems with the applicability of models have emerged.

Detailed studies of the OB stellar content in associations in the Milky Way and the Magellanic Clouds are now possible with CCD photometry (see Saken *et al.* 1992; Oey 1996a), and, in combination with stellar evolution models, they provide limits to the mechanical energy input rate. These rates have been used to compare LMC bubble observations with the predictions of the “standard” model (*i. e.*, a spherically symmetric shell evolving in a constant density medium). The comparisons indicate that the standard model cannot reproduce the properties of a number of well observed cases (Rosado 1986; Oey & Massey 1995; Oey 1996b). In particular, the collection of bubbles observed in the LMC exhibit two different sets of objects with conflicting size-velocity relations. Given that the observed shell sizes are well known, the problem can be reduced to the existence of objects with expansion velocities that are either too high or too low to be explained by the simple standard model. For the low velocity objects, the discrepancy could probably be explained by errors in the estimation of either the input wind power or ambient gas density (Oey 1996b). For the high velocity objects, however, the observed nebular expansion velocities ($V_{exp} \geq 25 \text{ km s}^{-1}$) are at least a factor of two larger than the expected values (Oey 1996b). Neither the density gradient in the disk of the LMC nor possible variations of the initial mass function (or non-coeval star formation) can resolve this discrepancy (Oey 1996b).

A possible solution to this problem can be associated with the fact that the LMC has a moderate inclination angle, of about 27° (Crampton 1979), and the shell are viewed with a nearly face-on orientation. For face-on galaxies, the density gradient along the z -direction can influence the bubble expansion along the line of sight, increasing the observed gas velocities. The effects of the gradient are more relevant in big spirals with a thin disk, but are less important in dwarf irregulars with extended HI layers (see discussion by Brinks & Walter 1998). However, the overall effect becomes certainly pronounced, even for dwarfs with very thick layers of H I, if one takes into account the presence of the parent giant molecular cloud (GMC) which gives birth to the perturbing stellar group and controls the initial bubble expansion: the high mass concentration within the parent GMC induces strong changes in the dynamics of shocks and can accelerate and generate fragmentation in the resulting shells (see Franco *et al.* 1989, 1990, 1997 and García-Segura & Franco 1996). A recent semi-analytical study of a model with a sharp density contrast indicates that the bubble kinematics could reach the required velocity values (Oey & Smedley 1998), and the presence of the parent cloud provides the required density gradient. In this paper we focus on the dynamics and observational manifestations of relatively young bubbles, with modest sizes (below 100 pc), which originate from associations embedded inside GMCs. The paper is organized as follows. Section 2 describes the basic input model and numerical scheme. Section 3 contains the results from numerical calculations, and these results are discussed in section 4.

2. The cloud density structure and model assumptions

For a spherically symmetric isothermal self-gravitating cloud in equilibrium, the gas density declines as r^{-2} (where r is the distance from the cloud center). For cylindrical (disk-like) self-gravitating clouds with infinite radius, on the other hand, the isothermal

density stratification along the z -axis varies as $\text{sech}^2(z/H)$ (where H is the scale height). Obviously, other cloud models with different morphologies result in different functional forms for the density stratifications. Here we use a simplified model to simulate the density distribution of a flattened, two-dimensional GMC. The 2-D stratification is defined in the cylindrical coordinate system (r, ϕ, z) , with the origin at the cloud center. The cloud has a constant density core, with density ρ_c , and the density decreases as a power-law until it reaches the value of the ambient medium, ρ_{ISM} . For simplicity, here we assume a constant value for ρ_{ISM} , and the initial GMC density distribution is then defined as

$$\rho = \begin{cases} \rho_c, & \text{for } \left(\frac{r}{R_c}\right)^2 + \left(\frac{z}{Z_c}\right)^2 \leq 1, \\ \rho_c \left[\left(\frac{r}{R_c}\right)^2 + \left(\frac{z}{Z_c}\right)^2\right]^{-w/2}, & \text{for } \left(\frac{r}{R_c}\right)^2 + \left(\frac{z}{Z_c}\right)^2 \leq \xi^{2/w}, \\ \rho_{ISM}, & \text{for } \left(\frac{r}{R_c}\right)^2 + \left(\frac{z}{Z_c}\right)^2 > \xi^{2/w}, \end{cases} \quad (1)$$

where $\xi = \rho_c/\rho_{ISM}$ is the ratio of the cloud core density to the ISM gas density, w is the power-law index, and R_c and Z_c are the characteristic scale heights for the cloud density distribution in the r and z -directions, respectively. The resulting maximum cloud extent along any of these axes is defined by $r_{cl} = R_c\xi^{1/w}$ and $z_{cl} = Z_c\xi^{1/w}$.

The appropriate range of values for the cloud parameters can be derived from observational results. For instance, using the spherically symmetric case ($R_c = Z_c$) we can derive the core radius from the condition that the observed shell mass, M_{obs} , is contained within the observed shell radius, R_{obs} . For a given core density, the observed mass is simply given by

$$M_{obs} = M_c + 4\pi \int_{R_c}^{R_{obs}} \rho(r)r^2 dr, \quad (2)$$

where M_c is the core mass, and the resulting core radius follows from the equation

$$\left(\frac{R_c}{R_{obs}}\right)^3 - \frac{3}{w} \left(\frac{R_c}{R_{obs}}\right)^w + \frac{3-w}{w} \frac{3M_{obs}}{4\pi R_{obs}^3 \rho_c} = 0. \quad (3)$$

For simplicity, we use $w = 2$ (which corresponds to a self-gravitating and isothermal sphere in the $R_c = Z_c$ case), and the radius R_{obs} is set equal to 40 pc. The mass M_{obs} is

considered in the range 2 to $5 \times 10^4 M_\odot$, to be consistent with the observed shell masses (Oey 1996b). The solution of equation (3), which is solved numerically at the beginning of the runs, is used as the characteristic scale height R_c for the two-dimensional models, and the characteristic scale in the z -direction is reduced to a half of this value, $Z_c = R_c/2$. Finally, we take the cloud core number density, n_c , as a free parameter, and explore density values in the range from 10 to 10^2 cm^{-3} . We designate the models as 'A' or 'B', depending on whether the resulting cloud mass M_{obs} is equal to 2 or $5 \times 10^4 M_\odot$, respectively. Thus, for a given core density value, they correspond to small and large clouds, respectively. The resulting GMC density distributions for both types of models, A and B, are illustrated in Figure 1, where the last isodensity contour represents the cloud boundary.

Assuming that the initial GMCs are in hydrostatic equilibrium, self-gravity defines the total pressure at the cloud center. Again, using the spherically symmetric model as an illustrative case, the total pressure at the cloud center is (García-Segura & Franco 1996)

$$p_c = \frac{16\pi}{9} G \rho_c^2 R_c^2. \quad (4)$$

The thermal pressure inside an adiabatic bubble, on the other hand, is

$$p_{in}(r_s) = \frac{(4.14\rho)^{1/3} L_0^{2/3}}{2\pi r_s^{4/3}}, \quad (5)$$

where r_s is the bubble radius, and L_0 is the mechanical energy input rate. The thermal pressure inside a bubble with radius equal to R_c (*i. e.*, a supershell emerging from the cloud core) exceeds the total pressure at the cloud center, $p_{in}(r_s = R_c) > p_c$, when the core densities are below the reference value

$$n_{\text{ref}} = \left(\frac{1}{4.14}\right)^{1/3} \left(\frac{9}{32\pi^2 G}\right)^{3/5} \left(\frac{L_0}{R_c^5}\right)^{2/5} \simeq 2 \times 10^4 L_{36}^{2/5} \left(\frac{1 \text{ pc}}{R_c}\right)^2 \text{ cm}^{-3}, \quad (6)$$

where $L_{36} = L_0/10^{36} \text{ erg s}^{-1}$. Thus, for densities below n_{ref} , one can neglect the cloud gravity and pressure during the early expansion and, for simplicity, we maintain only the

external ISM pressure, $p_{ISM} = k n_{ISM} T_{ISM}$, where k is the Boltzmann’s constant (the ambient gas temperature is maintained at 6×10^3 K° throughout the calculations).

The simulations are performed with the three-dimensional code described by Bisnovatyi-Kogan & Silich (1995) and Silich *et al.* (1996), which is based on the thin layer approximation. In the present set of calculations the energy input rate is assumed constant during the runs. Shell evaporation into the bubble due to thermal conduction is taken into account (see Silich *et al.* 1996), and this is the only source for mass injection into the cavity. The calculations of the X-ray luminosities are done with the table for the specific X-ray emissivities described by Suchkov *et al.* (1994). Several runs had been done taking into account possible fragmentation of the shell via the Rayleigh-Taylor (R-T) instability, as discussed by Silich & Tenorio-Tagle (1998). The model parameters used in the runs are summarized in Table 1.

3. The results

Figure 2 shows the resulting morphologies for models A and B (in the left and right panels, respectively). As expected, after expanding inside the constant density core, the remnant is elongated along the z -axis, where the density gradient is steepest. The deviation from the spherical morphology is already apparent after 2 Myr of evolution (Figs. 2b and 2e). At late evolutionary times, a dense, compressed ring-like belt is formed at the midplane of the cloud, as can be noticed in Fig. 2c (at 4 Myr) for model A2. In fact, model A2 presents a well defined hour-glass shape after 4 Myr, with two semi-spheres separated at midplane, as described in the analytical approach of Kontorovich & Pimenov (1997). Model B2, on the other hand, evolves more slowly in the higher density cloud, and after 4 Myr (Fig. 2f) it looks similar to model A2 after 2 Myr (Fig. 2b). Despite the large differences in

the z -direction between the elongated and spherical models, the midplane radii are similar for both types of models.

The evolutionary tracks for the two sets of cloud models are shown in Figures 3 and 4 (models A and B, respectively). For comparison, panels 3a and 4a show the radii and expansion velocities (solid and dotted lines, respectively) for the corresponding spherical bubble cases. Panels 3b, 3e, 4b, and 4e illustrate the kinematics for elongated bubbles, as they should be seen in a face-on galaxy: the solid lines represent the bubble radii in the midplane of the host galaxy (*i. e.*, along the r -axis), whereas the dotted lines correspond to the shell velocity in the z -direction. The kinematical properties for edge-on galaxies are shown in panels 3c, 3f, 4c, and 4f. In this case, the dotted lines represent the expansion velocities in the galactic midplane, and the solid and dashed lines show the bubble semi-axes along the plane and in the z -direction, respectively. For completeness, panels 3d and 4d show two runs similar to the ones displayed in 3b and 4b for the face-on configuration but allowing for shell fragmentation via the R-T instability. The evolutionary tracks are similar, except for a small increase in the expansion velocities for the cases allowing for the R-T instability.

The results presented in Figures 3 and 4 indicate that the expected expansion velocities for elongated bubbles in face-on galaxies are certainly larger than those derived from spherically symmetric models. The corresponding radii, however, are almost identical in both cases. A comparison between the results for small and large clouds (models A and B, respectively) show that the departures from the spherical case have well defined trends. For instance, the maximum value of the expansion velocity for smaller clouds is reached much earlier than in the case of larger clouds. Also, the velocity tracks for bubbles generated from small clouds are more peaked and can reach higher velocity values. Thus, as the cloud size increases, the peak velocity value decreases and the evolutionary track becomes shallower.

In all flattened cloud cases, however, the expansion velocity remains well above the one of the spherical model. For the particular cases that we show here, the expansion velocities can be higher than 20 km s^{-1} during the first 3 Myr of evolution.

These results raise the obvious question of how can one distinguish between spherical and elongated objects in a face-on galaxy. The simplest way to resolve this issue is to look for differences in the velocity distribution as a function of the bubble radius. To make the results independent of any particular model, we define the impact parameter a as the normalized distance from the bubble center. The normalization is done with the maximum shell radius, $a = r/R_{max}$, for the face-on configurations, and with the maximum z -extension, $a = z/Z_{top}$, for the edge-on cases. The z - and r -components of the expansion velocities are also normalized to the maximum projection velocity, U_{max} . The resulting velocity distributions for models A are shown in Figure 5 (the results for models B are qualitatively similar). The solid lines represent the spherical model A1, and the dotted and dashed lines correspond to the face-on and edge-on configurations of model A2, respectively. Panel 5a displays the velocity distribution after 2×10^5 yr, and panel 5b shows the same distribution after 1 Myr. At this time the elongated shell has an hour-glass form already, but the distributions for spherically symmetric and elongated face-on objects remain similar. A clear difference appears in the maximum value for the edge-on objects that shifts to the locations away from the center (dashed lines). The differences among the three cases are apparent only after 2 Myr, and the corresponding velocity distributions show distinctive features. The spherical case maintains its initial monotonic form and the edge-on case remains peaked off-center, but now the face-on case becomes double valued in regions close to the edge of the shell. This second velocity component near the shell boundaries becomes the kinematic feature that can help to recognize the existence of elongated bubbles seen face-on. For completeness, Figure 6 displays isovelocity contours for model A2 at 1 and 2 Myr of evolution, and as seen in face-on and edge-on galaxies.

Finally, Figure 7 illustrates the evolution of the X-ray luminosity, L_x , for the three models A. The bubble densities and temperatures drop faster in the elongated cases, and the resulting luminosities have a more rapid drop-off (also, the smaller thermal evaporation rates at the top shell regions prevent increase in the L_x values). The X-ray luminosity is stabilized as soon as the bubbles begin to expand in the external ISM. In contrast, the emission from the spherically symmetric case increases monotonically during the first 4 Myr of evolution. These differences are due to the differences in kinematical evolution, but the present results should be considered only lower limits because there are other important effects that have not been included here. For instance, the peak L_x values can be increased if one includes clumps (*e. g.* Arthur & Henney 1996; Silich *et al.* 1996) inside the hot remnant (the form of the curve, however, remains the same). Also, if one includes the presence of fragments in the stellar ejecta (Franco *et al.* 1993), the X-ray luminosity of the expanding shell is increased at each impact, and the light curve is modified accordingly. These issues require a more detailed study and will be explored in the near future.

4. Discussion and conclusions

In this paper we have presented a possible solution to the apparent discrepancy between the observed properties of some well observed LMC shells with high-velocities and the standard bubble model. Our present model assumes that these shells are driven by the energy injection from massive OB stars. This is a reasonable assumption for small bubbles, but may not be true for all observed holes and shells. In particular, the largest and most energetic observed superbubbles could be ascribed to a different, non-stellar, origin (such as the collision of high-velocity clouds with the gaseous disk; *e. g.* Tenorio-Tagle *et al.* 1987; Santillán *et al.* 1999).

The issue at hand is the role of the parent GMC in the kinematical properties of young bubbles when viewed, as in the case of the LMC, at an almost face-on orientation. For simplicity, our 2-D numerical calculations consider the presence of flattened GMCs but do not include the z -gradient of the main gaseous disk. Nonetheless, the results already indicate that bubbles blowing out of these flattened clouds can reach a high degree of asymmetry on a short timescale (during the first million years of expansion), with z -velocities in the range of the observed high-velocity cases. This is in line with the semi-analytical results for a sharp density contrast discussed by Oey & Smedley (1998), but a steep density gradient is not really required. We find that for moderate values of the GMC flatness, the expansion velocities at the top could easily exceed those expected from spherical models by a factor of two or more. This scheme then provides a possible explanation of the observed high-velocity cases, with $V_{exp} \geq 25 \text{ km s}^{-1}$ and radii of several tens of parsecs (Rosado *et al.* 1981, 1982; Rosado 1986; Oey 1996b).

With respect to the resulting X-ray luminosities, the present version of the model cannot explain the X-ray excess that is often observed in high-velocity superbubbles (Chu & Mac Low 1990; Rosado *et al.* 1993). To explore this issue one requires to consider the destruction of pre-existing gas clumps (Arthur & Henney 1996; Silich *et al.* 1996), or to include the interaction of fragmented ejecta with the expanding shell (Franco *et al.* 1993). Each of these mechanisms can increase the value of L_x during different moments of the evolution.

The remarkable difference in the velocity distributions as a function of impact parameter for face-on and edge-on galaxies, illustrated in Figure 5, indicates that one can differentiate elongated and spherical shell in both face-on and edge-on galaxies. Spectral line splitting at the periphery of nebular shells and off-center peak velocity values are indicators of elongated morphologies in the face-on and edge-on cases, respectively. Observational

studies with adequate spatial resolution are needed to verify these predictions in nearby galaxies with different orientations.

This is the same type of model that is commonly applied to explain fast starburst-driven outflows in external galaxies (see review by Heckman 1997), and we have only added the expected density structure at the initial stages of outflow evolution. Our results indicate that the presence of star-forming clouds produce asymmetries in short time scales, and shell projection effects are important when comparing models with observed shells. Future studies including the destructive effects of expanding HII regions (*e. g.* Franco *et al.* 1994), and the re-acceleration generated by individual supernova explosions (*e. g.* Tenorio-Tagle *et al.* 1991; Franco *et al.* 1991; Arthur & Falle 1993; Arthur & Henney 1996), will certainly improve our understanding of the early phases of superbubble evolution.

Acknowledgments It is a big pleasure to thank Sally Oey and Margarita Rosado for helpful discussions on LMC bubbles and shells, and Jane Arthur for useful comments. We also thank Elias Brinks, David Thilker, and Rene Walterbos for information on superbubble population of spirals and irregulars. Special thanks to Steve Shore and an anonymous referee for very useful suggestions that greatly improved the final version of this paper. JF acknowledges partial support from DGAPA-UNAM grant IN130698, CONACyT grants 400354-5-4843E and 400354-5-0639PE, and a R&D CRAY Research grant. SAS acknowledges support from a Royal Society grant for joint projects with the former Soviet Union States, and the staff of IoA and RGO in Cambridge, where this study has been initiated. He thanks the Instituto de Astronomía-UNAM for support, hospitality, and friendly assistance during his visit to Mexico.

References

Arthur, J. & Falle, S. A. E. G. 1993, MNRAS, 341, L63

- Arthur, J. & Henney, W. 1996, *ApJ*, 457, 752
- Avedisova, V. S. 1972, *SovAstron*, 15, 708
- Bisnovatyi-Kogan, G.S. & Blinnikov, S.I. 1982, *SovAstron*, 26, 530
- Bisnovatyi-Kogan, G.S. & Silich, S.A. 1995, *RevModPhys*, 67, 661
- Boulesteix, J., Courtes, G., Laval, A., Monnet, G. & Petit, A. 1974, *A&A*, 37, 33
- Brinks, E. 1994, in *Violent Star Formation: from 30 Doradus to QSOs*, ed. G. Tenorio-Tagle (Cambridge: Cambridge Univ. Press), 145
- Brinks, E. & Bajaja, E. 1986, *A&A* 169, 14
- Brinks, E. & Walter, F. 1998, in *The Magellanic Clouds and Other Dwarf Galaxies*, ed. T. Richtler & J. Braun (Aachen: Shaken Verlag), in press
- Chu, Y.-H. & Mac Low, M.-M. 1990, *ApJ*, 365, 510
- Comeron, F. 1997, *A&A*, 326, 1195
- Crampton, D. 1979, *ApJ*, 230, 717
- Davies, R. D., Elliot, K. H. & Meaburn, J. 1976, *MNRAS*, 81, 89
- Ehlerova S., Palous, J., Theis, Ch. & Hensler, G. 1997, *A&A*, 328, 121
- Elmegreen, B. G. & Chiang, W. H. 1982, *ApJ*, 253, 666
- Ferriere, K., Mac Low, M.-M. & Zweibel, E. 1991, *ApJ*, 375, 239
- Franco, J., Ferrara, A., Różyczka, M., Tenorio-Tagle, G. & Cox, D. P. 1993, *ApJ*, 407, 100
- Franco, J., Ferrini, F., Ferrara, A. & Barsella, B. 1991, *ApJ*, 366, 443

- Franco, J., Plewa, T. & Garcia-Segura, G. 1997, in *Starburst Activity in Galaxies*, ed. J. Franco, R. Terlevich & A. Serrano, *RevMexAA Conf. Series*, 6, 172
- Franco, J., Shore, S. N. & Tenorio-Tagle, G. 1994, *ApJ*, 436, 795
- Franco, J., Tenorio-Tagle, G. & Bodenheimer, P. 1989, *RevMexAA*, 18, 65
- Franco, J., Tenorio-Tagle, G. & Bodenheimer, P. 1990, *ApJ*, 349, 126
- Franco, J., Tenorio-Tagle, G., Bodenheimer, P. & Różyczka, M. 1991, *PASP*, 103, 803
- García-Segura, G. & Franco, J. 1996, *ApJ*, 469, 171
- García-Segura, G. & Mac Low, M.-M. 1995a, *ApJ*, 455, 145
- García-Segura, G. & Mac Low, M.-M. 1995b, *ApJ*, 455, 160
- Hartquist, T.W., Dyson, J.E., Pettini, M. & Smith, L.J. 1986, *MNRAS*, 221, 715
- Heckman, T. 1997, in *Starburst Activity in Galaxies*, ed. J. Franco, R. Terlevich & A. Serrano, *RevMexAAp (Conf. Series)*, 6, 156
- Heiles, C. 1979, *ApJ*, 229, 533.
- Hindman, J. V. 1967, *AustJPhys*, 20, 147
- Kontorovich, V.M. & Pimenov, S.F. 1997, *SolPhys*, 172, 93
- Lozinskaya, T. A. & Sitnik, T. G. 1988, *AstronZhLett*, 14, 240
- Mac Low, M.-M. & McCray, R. 1988, *ApJ*, 324, 776
- Mac Low, M.-M., McCray, R. & Norman, M. L. 1989, *ApJ*, 337, 141
- Mashchenko, S., Thilker, D. & Braun, R. 1999, *A&A*, 343, 352

Meaburn, J. 1980, MNRAS, 192, 365

McGee, R. X. & Milton, J. A. 1966, AustJPhys, 19, 343

Moreno, E., Alfaro, E. J. & Franco, J. 1999, ApJ, in press

Oey, M. S. & Massey, P. 1995, ApJ, 452, 210

Oey, M. S. 1996a, ApJ, 465, 231

Oey, M. S. 1996b, ApJ, 467, 666

Oey, M. S. & Smedley, S. A. 1998, AJ, 116, 1263

Palouš, J. 1992, in Evolution of Interstellar Matter and Dynamics of Galaxies, ed. J. Palouš, W.B. Burton & P.O. Lindblad (Cambridge: Cambridge Univ. Press), 65

Pellet, A., Astier, N., Viale, A., Courtes, G., Maucherat, A., Monnet, G. & Simien, F. 1978, A&ASuppl, 33, 439

Pikel'ner, S. B. 1968, ApLett, 2, 97

Rosado, M. 1986, A&A, 160, 211

Rosado, M., Georgelin, Y. P., Georgelin, Y. M., Laval, A. & Monnet, G. 1981, A&A, 97, 342

Rosado, M., Georgelin, Y. M., Georgelin, Y. P., Laval, A. & Monnet, G. 1982, A&A, 115, 61

Rosado, M., Le Coarer, E., Laval, A. & Georgelin, Y. P. 1993, RevMexAA, 27, 41

Saken, J.M., Shull, J.M., Garmany, C.D., Nichols-Bohlin, J. & Fesen, R.A. 1992, ApJ, 397, 537

- Santillán, A., Franco, J., Martos, M. & Kim, J. 1999, ApJ, in press
- Silich, S. A. 1992, Ap&SS, 195, 317
- Silich, S. A., Franco, J., Palous, J & Tenorio-Tagle, G. 1996, ApJ, 468, 722
- Silich, S. A. & Tenorio-Tagle, G. 1998, MNRAS, 299, 249
- Sivan, J. P. 1977, PhD Thesis, Univ. of Provence, France
- Suchkov, A. A., Balsara, D. S., Heckman, T. M. & Leitherer, C. 1994, ApJ, 430, 511
- Tenorio-Tagle, G. & Bodenheimer, P. 1988, ARAA, 26, 145
- Tenorio-Tagle, G., Franco, J., Różyczka, M. & Bodenheimer, P. 1987, A&A, 179, 219
- Tenorio-Tagle, G., Różyczka, M. & Bodenheimer, P. 1990, A&A, 237, 207
- Tenorio-Tagle, G., Różyczka, M., Franco, J. & Bodenheimer, P. 1991, MNRAS, 251, 318
- Thilker, D.A., Braun, R. & Walterbos, R. 1998, A&A, 332, 429
- Thilker, D.A. 1998, in *Interstellar Turbulence*, ed. J. Franco & A. Carramiñana
(Cambridge: Cambridge Univ. Press) (in press)
- Tomisaka, K. 1990, ApJ, 361, L5
- Tomisaka, K. 1998, MNRAS, 298, 797
- Weaver, R., McCray, R., Castor, J., Shapiro, P. & Moore, R. 1977, ApJ, 218, 377
- Westerlund, B. E. & Mathewson, D. S. 1966, MNRAS, 131, 371

Table 1

Model parameters (with $w = 2$)

Model	n_c cm^{-3}	n_{ISM} cm^{-3}	M_f $10^4 M_\odot$	R_c pc	Z_c pc	R_{cl} pc	L_{OB} $10^{36} \text{ erg s}^{-1}$
A1	2.4	2.4	2	-	-	-	5
A2	10	0.2	2	12.6	6.3	89.5	5
A3	100	0.2	2	3.7	1.8	82.1	5
B1	5.9	5.9	5	-	-	-	5
B2	10	0.2	5	22.5	11.25	159.0	5
B3	100	0.2	5	5.9	2.95	132.5	5

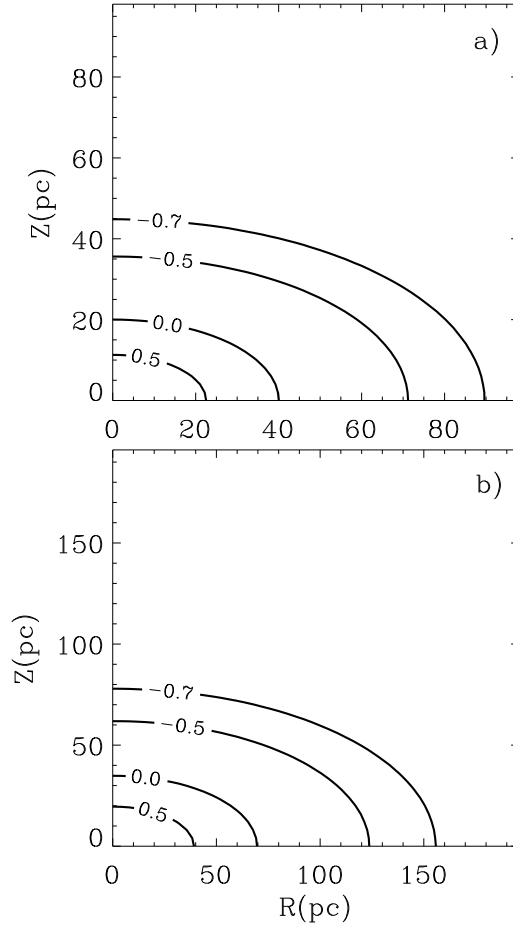


Fig. 1.— The gas density distribution for the model GMCs. Panels (a) and (b) show the isodensity contours for models A2 and B2, respectively. The value of $\log n$ is indicated at each contour.

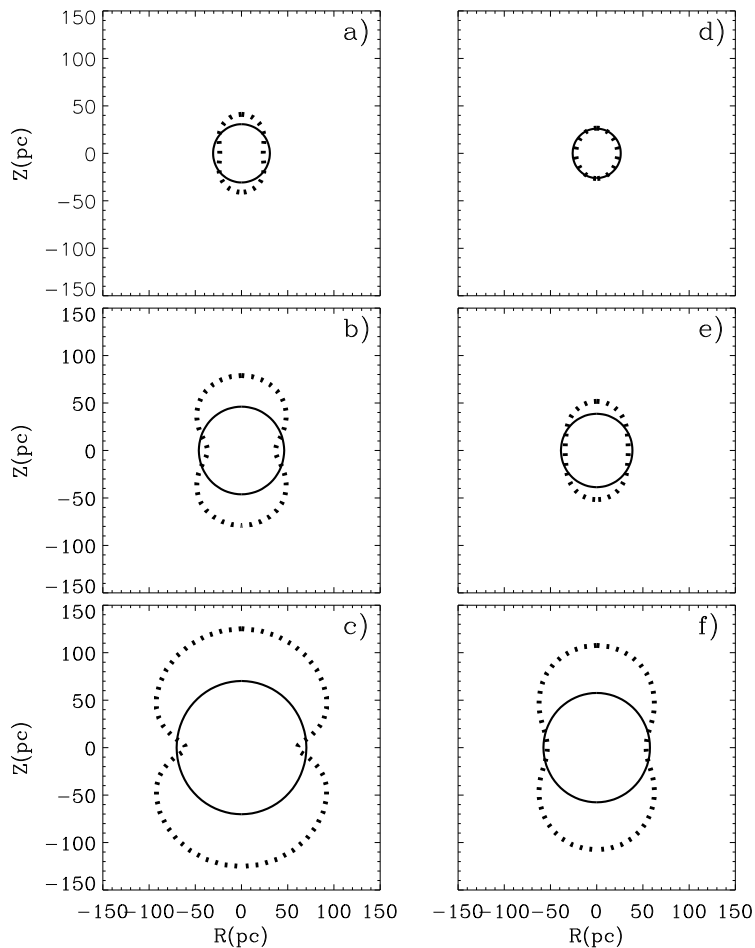


Fig. 2.— Superbubble shapes for models A1 and A2 (left panels), and B1 and B2 (right panels). The panels show the evolution at $t = 1$ Myr (a and d), 2 Myr (b and e), and 4 Myr (c and f). The solid lines represent the spherical bubbles, A1 and B1, and the dotted lines correspond to models A2 and B2.

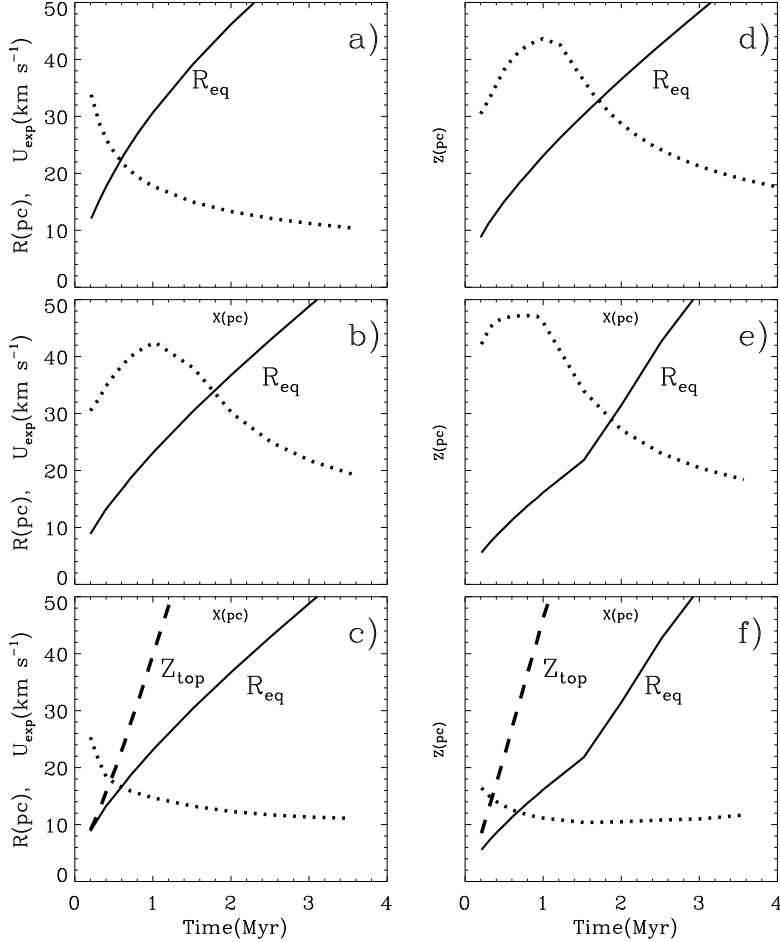


Fig. 3.— The expansion velocities and radii for models A. a) Spherical model A1. b) Model A2 as seen in a face-on galaxy. c) Model A2 as seen in an edge-on galaxy. d) Model A2 including shell fragmentation due to R-T instability. e) Model A3 for a face-on galaxy. f) Model A3 for an edge-on galaxy. The solid lines are the shell radii along the plane of the galaxy, and the dashed lines are the top z -extensions. Dotted lines for panels a, b, d and e are the top expansion velocities along the z -axis. Dotted lines for panels c and f are the expansion velocities at the bubble equator.

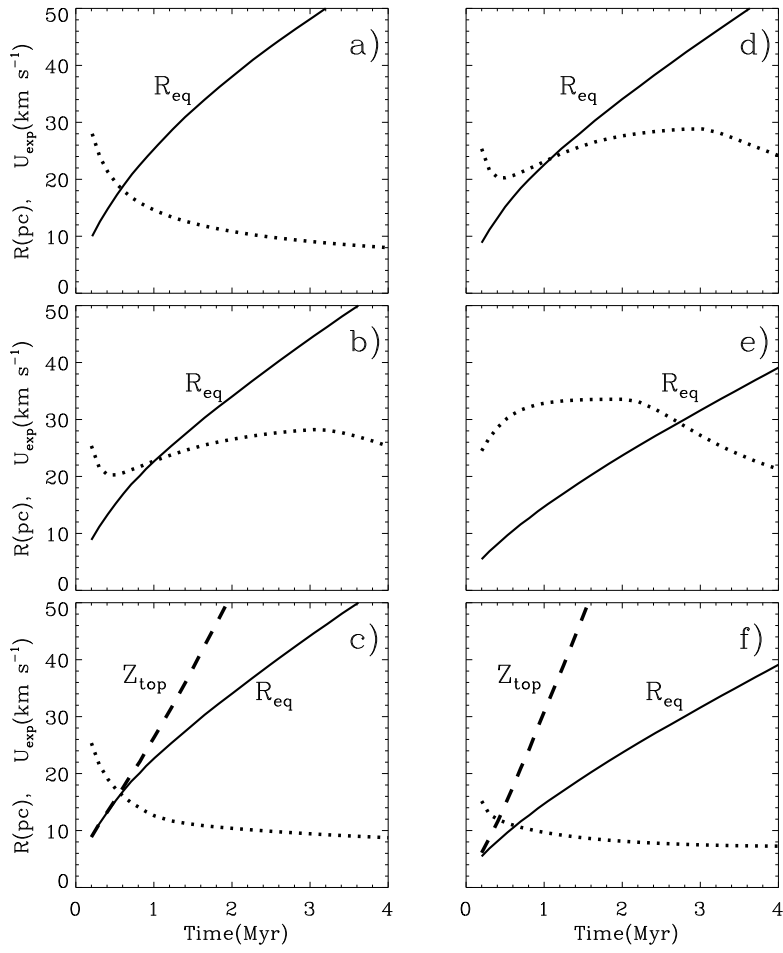


Fig. 4.— Same as Figure 3, but for models B.

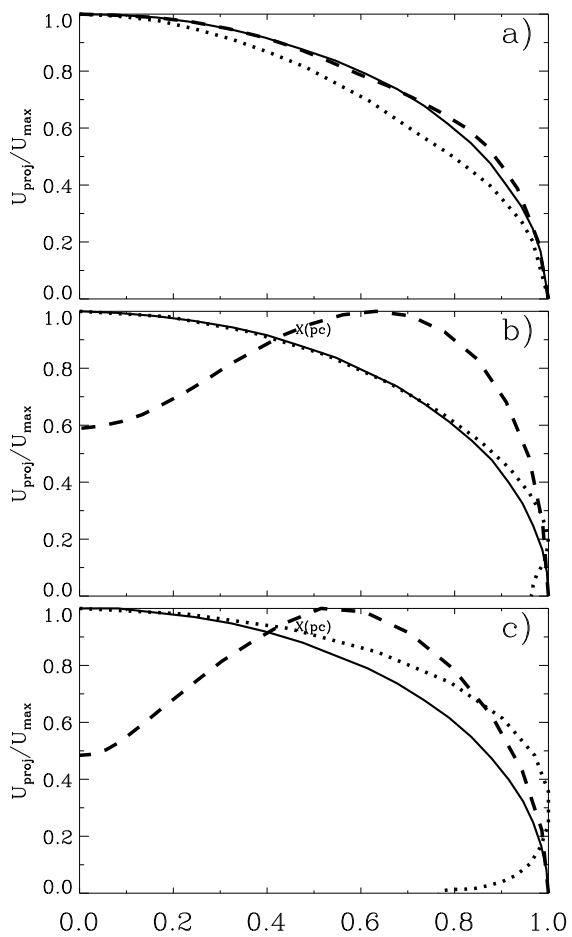


Fig. 5.— The normalized projected velocities^a as a function of the impact parameter a for models A. a) $t = 2 \times 10^5$ yr, b) 1 Myr, and c) 2 Myr. The solid lines present the spherical model A1, the dotted lines show the face-on case A2, and the dashed lines are for the edge-on case A2.

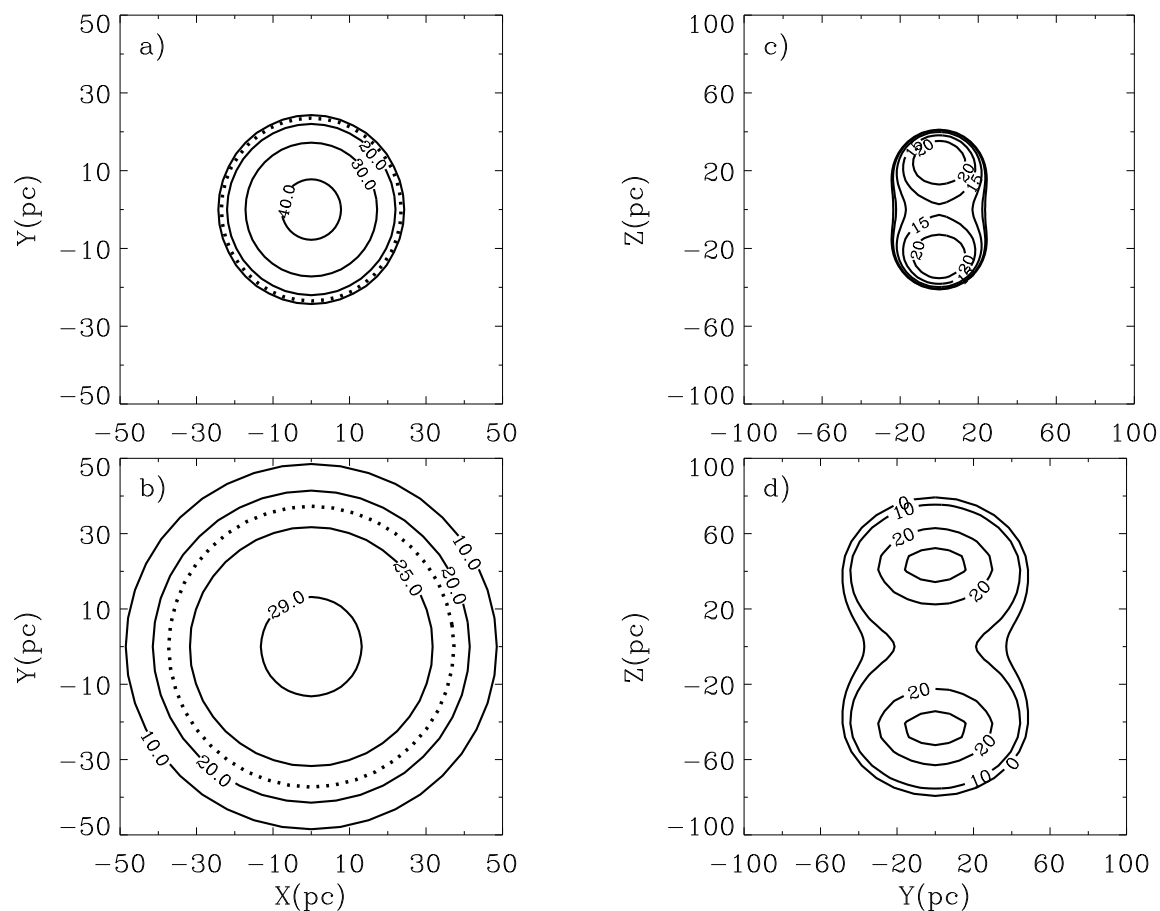


Fig. 6.— Isovelocity maps for model A2. Panels a) and b) show the results as seen in a face-on galaxy at 1 and 2 Myr, respectively. Panels c) and d) are the same for an edge-on galaxy. The dotted lines represent the zero velocity contours (*i. e.*, the bubble cross-section at the midplane of the cloud).

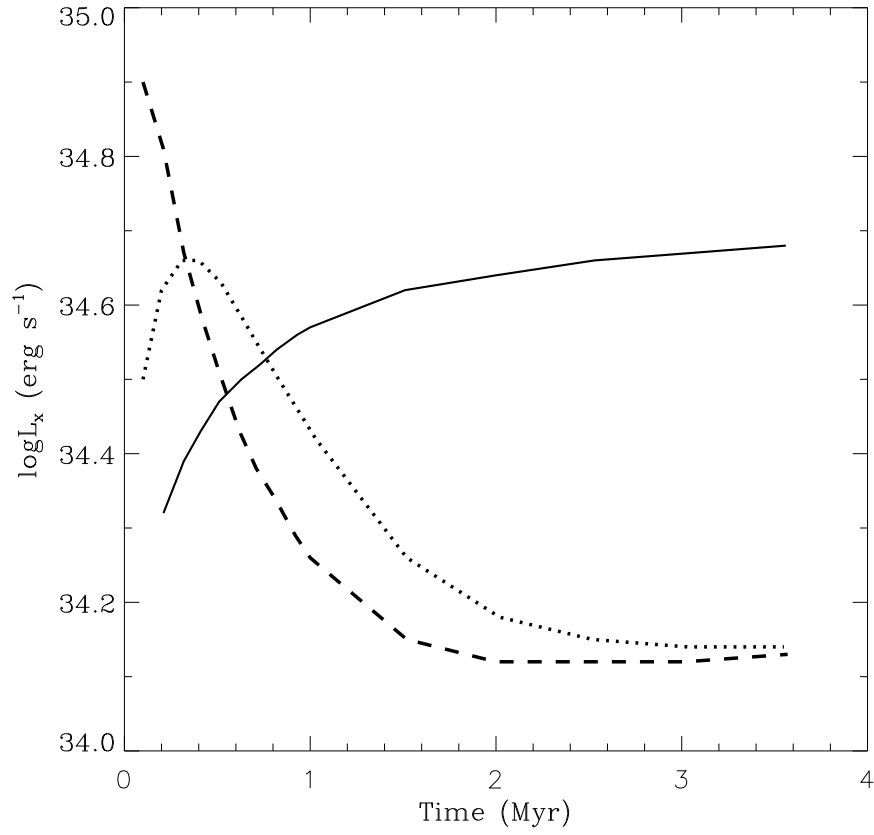


Fig. 7.— The X-ray luminosities for models A. The solid line presents the spherical model A1, the dotted line is for model A2, and the dashed line is for model A3.